

Research Article

Effects of Sintering Temperature on the Morphology and Photoluminescence of Eu^{3+} Doped Zinc Molybdenum Oxide Hydrate

Bao-gai Zhai,¹ Qing-lan Ma,² Long Yang,¹ and Yuan Ming Huang¹ 

¹School of Mathematics and Physics, Changzhou University, Jiangsu 213164, China

²School of Electronics and Information, Nantong University, Jiangsu 226019, China

Correspondence should be addressed to Yuan Ming Huang; dongshanisland@126.com

Received 9 October 2017; Revised 5 February 2018; Accepted 19 February 2018; Published 21 March 2018

Academic Editor: Oscar Perales-Pérez

Copyright © 2018 Bao-gai Zhai et al. This is an open access article distributed under the Creative Commons Attribution License, which permits unrestricted use, distribution, and reproduction in any medium, provided the original work is properly cited.

Synthesis of shape controlled and rare-earth doped ZnMoO_4 nanostructures on a large scale with low costs is a present challenge in nanotechnology. The precursor of Eu^{3+} doped zinc molybdenum oxide hydrate ($\text{Zn}_5\text{Mo}_2\text{O}_{11}\cdot 5\text{H}_2\text{O}$) was synthesized at room temperature via the coprecipitation method. The influences of the sintering temperature on the microstructures and photoluminescence (PL) of the precursor were investigated by means of X-ray diffraction, scanning electron microscopy, thermal gravimetry, differential scanning calorimetry, energy dispersive X-ray spectroscopy, diffuse reflectance spectroscopy, and PL spectrophotometry. It is found that Eu^{3+} doped ZnMoO_4 nanostructures can be derived by sintering the precursor at a relatively low temperature of about 400°C. Our results have demonstrated that Eu^{3+} doped ZnMoO_4 nanostructures can be cost-effectively derived by sintering the precursor at a relatively low temperature.

1. Introduction

Zinc molybdate tetraoxide (ZnMoO_4), which can be utilized as cryogenic scintillating bolometers for neutrinoless double beta decay detection [1–3], has attracted interest in the last years as the host material for rare-earth ions [4–8]. As is well known, triclinic ZnMoO_4 is composed of a series of distorted Mo-O tetrahedrons, Zn-O pentahedrons, and Zn-O octahedrons. In a distorted Mo-O tetrahedron, the Mo atom is surrounded by four oxygen atoms. Similarly, the Zn atom in a Zn-O pentahedron is surrounded by five oxygen atoms, and the Zn atom in a Zn-O octahedron is surrounded by six oxygen atoms [9]. After substituting the Zn^{2+} sites in ZnMoO_4 , the rare-earth ions in the ZnMoO_4 crystal lattice can give off the characteristic emissions of the rare-earth dopants upon ultraviolet excitation. Therefore, triclinic ZnMoO_4 is considered as an excellent host material for rare-earth dopants. For example, Zhou et al. prepared red phosphor Eu^{3+} doped ZnMoO_4 for light-emitting diode application by solid-state reaction method at 900°C [4]; Chengaiah et al. synthesized white phosphor Dy^{3+} doped

ZnMoO_4 using the solid-state reaction method at 900°C [7]; Ju et al. prepared green phosphor Tb^{3+} doped ZnMoO_4 via sintering precipitation at 800°C [8]. Although characteristic emissions of the rare-earth dopants can be clearly identified in the rare-earth doped ZnMoO_4 , the high temperature treatment makes the reported approaches suffer from the drawback of being highly energy-consuming [4, 7, 8, 10]. Thus synthesis of rare-earth doped ZnMoO_4 nanostructures on a large scale with low costs is a present challenge in nanotechnology, and it is necessary to develop an energy-saving and cost-effective route to prepare rare-earth doped ZnMoO_4 .

The precipitation synthesis is an energy-saving and cost-effective method for mass-producing nanomaterials [11]. Eu^{3+} is a typical rare-earth dopant; the most prominent feature of Eu^{3+} is its red emission at 616 and 628 nm due to its ${}^5\text{D}_0 \rightarrow {}^7\text{F}_2$. So we selected Eu^{3+} as a representative of rare-earth dopants to study the photoluminescence (PL) properties of rare-earth doped ZnMoO_4 . Normally the dopant concentration of rare-earth element in ZnMoO_4 varies in the range of 0.1–30 mol% [4–8]. It is known that the intensity of

the characteristic emissions of Eu^{3+} in host materials depends on the Eu^{3+} concentration, but no much new insight can be provided by varying the concentration of Eu^{3+} dopant except PL quenching at high doping concentration [4, 8]. This is the reason why we simply selected 1 mol% of Eu^{3+} as dopant in the host materials. In this paper, we reported that Eu^{3+} doped ZnMoO_4 nanostructures could be derived by sintering the precursor of Eu^{3+} doped zinc molybdenum oxide hydrate ($\text{Zn}_5\text{Mo}_2\text{O}_{11}\cdot 5\text{H}_2\text{O}$, ZMO) at a relatively low temperature of about 400°C . The precursor Eu^{3+} doped ZMO was synthesized via the precipitation method at room temperature. The effects of the sintering temperature on the morphology and PL of the precursor were investigated.

2. Materials and Characterizations

The precursor of Eu^{3+} doped ZMO was synthesized at room temperature via the precipitation method. Hexaammonium heptamolybdate tetrahydrate $[(\text{NH}_4)_6\text{Mo}_7\text{O}_{24}\cdot 4\text{H}_2\text{O}]$, zinc nitrate hexahydrate $[\text{Zn}(\text{NO}_3)_2\cdot 6\text{H}_2\text{O}]$, europium nitrate hexahydrate $[\text{Eu}(\text{NO}_3)_3\cdot 6\text{H}_2\text{O}]$, and sodium hydroxide (NaOH) were used as the starting materials. In a cleaned beaker, aqueous solution A was prepared by dissolving $(\text{NH}_4)_6\text{Mo}_7\text{O}_{24}\cdot 4\text{H}_2\text{O}$ (0.01 mol) and $\text{Eu}(\text{NO}_3)_3\cdot 6\text{H}_2\text{O}$ (0.0007 mol) into 100 mL deionized water. In a similar way, aqueous solution B was prepared by dissolving $\text{Zn}(\text{NO}_3)_2\cdot 6\text{H}_2\text{O}$ (0.175 mol) into 100 mL deionized water. Under vigorous stirring with a magnetic bar, aqueous solution of NaOH (0.08 mol) was dropped into solution A in order to hydrolyze $(\text{NH}_4)_6\text{Mo}_7\text{O}_{24}$. White precipitate was formed in the beaker when solution B was slowly added to the hydrolyzed solution. The pH value of the solution in the beaker was adjusted to 7 by adding extra aqueous solution of NaOH. The precipitate was filtered, washed with water, and dried in an oven at 60°C for overnight. The dried precipitate, which was identified as Eu^{3+} doped ZMO, was divided into four shares for subsequent sintering in an air-filled furnace at 200, 400, 600, and 800°C for 2 h, respectively. The dopant concentration of Eu^{3+} in each sample was 1 mol%.

X-ray diffraction (XRD) curves were recorded on an X-ray diffractometer (D/max 2500 PC, Rigaku Corporation, Japan) using $\text{Cu K}\alpha$ radiation ($\lambda = 0.15405\text{ nm}$). The voltage applied to the Cu target in the XRD machine was 40 kV. The scanning electron microscope (SEM) (S-4800, Hitachi, Japan) was employed to analyze the morphology and elemental composition of the resultant compounds. The accelerating voltage applied to the electron gun in the SEM was 15 kV. The SEM was coupled with a silicon drifted detector as the X-ray analyzer for the energy dispersive X-ray spectroscopic (EDX) analysis. The weight change and heat flow of the dried precipitate were measured with a simultaneous thermal analyzer (Pyris Series STA 6000, Perkin Elmer). Al_2O_3 crucibles were used as the sample containers in the thermogravimetry (TG) analysis and the differential scanning calorimetry (DSC) analysis. The N_2 purge gas flow rate was approximately 19.8 mL/min. The samples were run using a scanning rate of $10^\circ\text{C}/\text{min}$ in the TG and DSC characterizations.

The diffuse reflectance spectrum of Eu^{3+} doped ZnMoO_4 was measured with a UV-vis spectrometer (UV3600, Shimadzu). The PL spectra of the resultant compounds were recorded with a spectrophotometer (Tianjin Gangdong Ltd., China). The 325 nm laser line from a helium-cadmium laser was utilized as the excitation source for the PL measurement. The PL lifetime measurement of Eu^{3+} doped ZnMoO_4 was performed at room temperature on a picosecond fluorescence lifetime spectrometer (LifeSpec II, Edinburgh Instruments). The 375 nm excitation source was supplied with a picosecond pulsed diode laser, which was operating at a repetition rate of 10 MHz and having a pulse width of 55 ps. The photoexcitation spectrum of Eu^{3+} doped ZnMoO_4 was measured with the fluorescence spectrometer LS45 (Perkin Elmer) by fixing the monitoring wavelength at 615 nm.

3. Results and Discussions

3.1. XRD Analysis. Figure 1 depicts the XRD curves of the as-prepared precursor before (a) and after thermal annealing at 200°C (b). The duration of thermal annealing is 2 h, and the materials in (a) and (b) are Eu^{3+} doped ZMO. The XRD curve of the as-prepared precursor is presented in Figure 1(a), where one can observe well-defined peaks corresponding to the single phase of ZMO. The diffraction peaks at 12.266 , 17.170 , 23.466 , 26.578 , 29.062 , 31.680 , 33.562 , 33.955 , 34.714 , and 38.489° can be assigned to the reflections from the 003, 101, 104, 015, 110, 113, 107, 021, 202, and 116 crystallographic planes of ZMO (JCPDS No. 30-1486), respectively. The standard XRD data of hexagonal ZMO is shown at the bottom of Figure 1 for comparison (JCPDS No. 30-1486). According to the JCPDS No. 30-1486, the lattice parameters of standard hexagonal ZMO are known as $a = 0.6136\text{ nm}$ and $c = 2.16\text{ nm}$. The lattice parameters of the Eu^{3+} doped ZMO can be determined by whole pattern fitting and Rietveld refinement of the XRD curves in Figure 1. As listed by the second row in Table 1, the lattice parameters of the Eu^{3+} doped ZMO without annealing are found to be $a = b = 0.6100\text{ nm}$, $c = 2.164\text{ nm}$, $\alpha = \beta = 90^\circ$, and $\gamma = 120^\circ$. It can be seen clearly that the lattice parameters of Eu^{3+} doped ZMO agree well with those of standard ZMO. Figure 1(b) shows that the Eu^{3+} doped ZMO preserves its crystal structure upon heating at 200°C for 2 h. The lattice parameters of the annealed precursor are listed as the third row in Table 1. Using Scherrer equation, we calculated the mean grain sizes of the crystalline domains as a function of the annealing temperature. The shape factor in the Scherrer equation took the typical value of 0.9. On the basis of the (015) peak broadening in Figure 1, the mean sizes were derived to be around 74.2 and 54.4 nm for the as-prepared precursor before and after thermal annealing at 200°C , respectively.

Figure 2 represents the XRD spectra of Eu^{3+} doped ZnMoO_4 compounds obtained by thermally annealing the precursor at 400°C (a), 600°C (b), and 800°C (c) for 2 h. As marked by the vertically aligned dash lines, the 12 diffraction peaks are located at $2\theta = 13.219$, 15.994 , 19.235 , 22.877 , 24.179 , 26.129 , 26.633 , 27.597 , 30.054 , 32.253 , 33.388 , and 33.876° . These 12 peaks in Figure 2 can be assigned to the reflections

TABLE 1: Lattice parameters of Eu^{3+} doped $\text{Zn}_5\text{Mo}_2\text{O}_{11}\cdot 5\text{H}_2\text{O}$ and Eu^{3+} doped ZnMoO_4 determined by whole pattern fitting and Rietveld refinement.

Precursor	a (nm)	b (nm)	c (nm)	α ($^\circ$)	β ($^\circ$)	γ ($^\circ$)	Phase
As-prepared	0.6100	0.6100	2.164	90	90	120	$\text{Zn}_5\text{Mo}_2\text{O}_{11}\cdot 5\text{H}_2\text{O}$
Annealed at 200 $^\circ\text{C}$	0.6110	0.6110	2.163	90	90	120	$\text{Zn}_5\text{Mo}_2\text{O}_{11}\cdot 5\text{H}_2\text{O}$
Annealed at 400 $^\circ\text{C}$	0.8372	0.9702	0.6964	106.80	101.81	96.80	Triclinic ZnMoO_4
Annealed at 600 $^\circ\text{C}$	0.8364	0.9689	0.6960	106.86	101.77	96.75	Triclinic ZnMoO_4
Annealed at 800 $^\circ\text{C}$	0.8353	0.9673	0.6954	106.84	101.76	96.73	ZnMoO_4 (primary)

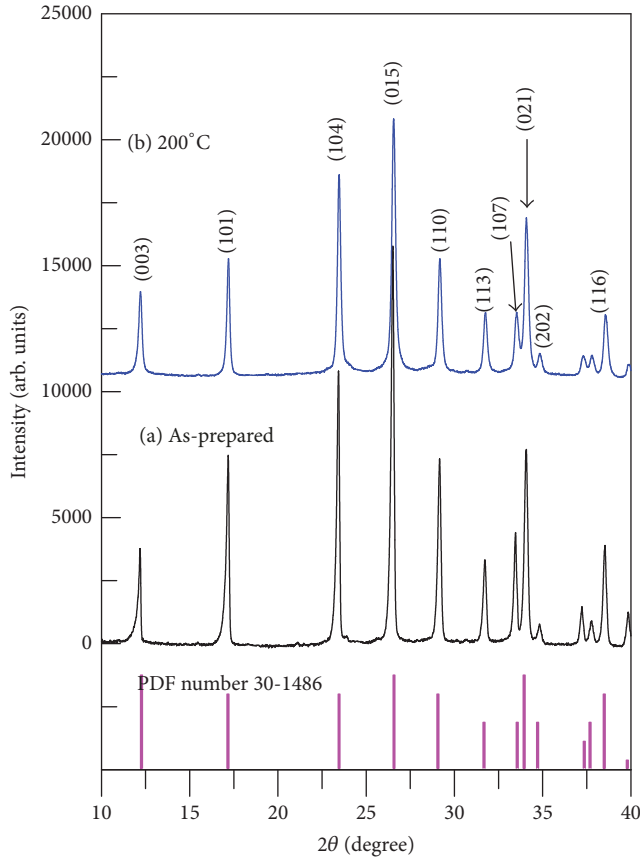


FIGURE 1: XRD curves of the precursors before (a) and after thermal annealing at 200 $^\circ\text{C}$ (b). The materials in (a) and (b) are Eu^{3+} doped $\text{Zn}_5\text{Mo}_2\text{O}_{11}\cdot 5\text{H}_2\text{O}$.

from the $\bar{1}10$, 110 , 011 , $1\bar{2}1$, 120 , $0\bar{1}2$, $\bar{2}20$, $2\bar{1}1$, $\bar{2}\bar{2}1$, 012 , 300 , and $\bar{1}21$ planes of triclinic ZnMoO_4 , respectively [4, 5, 7, 8, 10, 11]. The standard XRD data of triclinic ZnMoO_4 are presented at the bottom of Figure 2 for comparison. The lattice parameters of standard triclinic ZnMoO_4 are $a = 0.9625$ nm, $b = 0.6965$ nm, $c = 0.8373$ nm, $\alpha = 103.28^\circ$, $\beta = 96.30^\circ$, and $\gamma = 106.72^\circ$ (JCPDS No. 35-0765). In our case, the lattice parameters of Eu^{3+} doped ZnMoO_4 can be determined by whole pattern fitting and Rietveld refinement, as listed as the fourth, fifth, and sixth rows in Table 1. It is clear that the lattice parameters of Eu^{3+} doped ZnMoO_4 vary a little bit away from the standard parameters when the annealing temperature increases from 400 to 800 $^\circ\text{C}$. A careful check on the XRD curves (a)–(c) reveals that the resultant ZnMoO_4

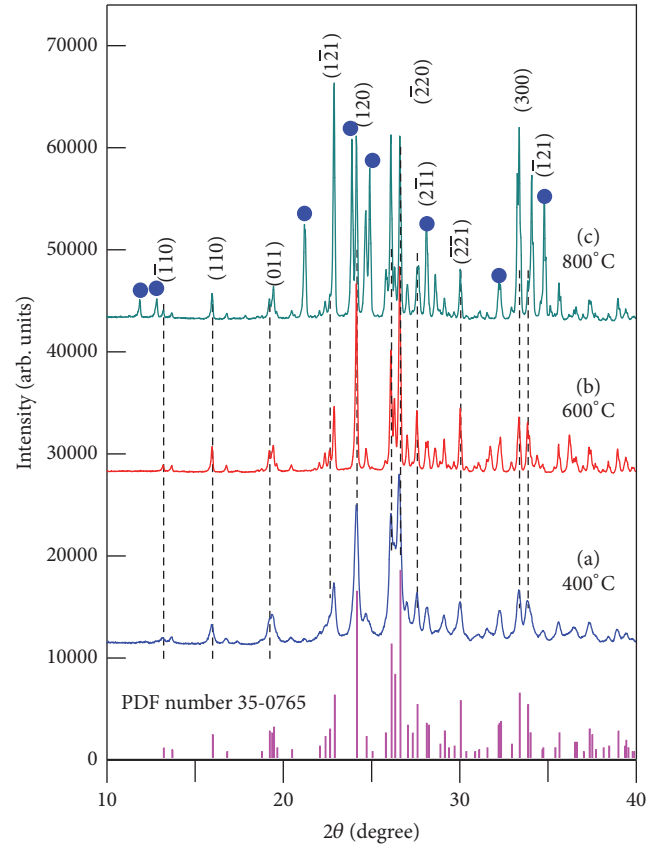


FIGURE 2: XRD curves of Eu^{3+} doped ZnMoO_4 compounds obtained by thermal annealing the precursor at 400 $^\circ\text{C}$ (a), 600 $^\circ\text{C}$ (b), and 800 $^\circ\text{C}$ (c) for 2 h.

is in its pure triclinic phase when the sintering temperatures are 400 and 600 $^\circ\text{C}$. But the case is changed when the sintering temperature is elevated to 800 $^\circ\text{C}$. A secondary phase appears, as marked with the solid blue dots upon the XRD curve (c). The diffraction peaks of the secondary phase are located at 11.837° , 11.800° , 21.187° , 23.836° , 24.850° , 28.126° , and 34.756° , which are consistent with those of $\text{Zn}_3\text{Mo}_2\text{O}_9$ (JCPDS No. 30-1484). These results demonstrate that the secondary phase $\text{Zn}_3\text{Mo}_2\text{O}_9$ coexists with the primary phase ZnMoO_4 when the sintering temperature is elevated to 800 $^\circ\text{C}$. On the basis of the (120) peak broadening in Figure 2, the mean sizes of Eu^{3+} doped ZnMoO_4 are calculated to be 42.7, 270.7, and 812.1 nm for the precursors annealed at 400, 600, and 800 $^\circ\text{C}$, respectively. It is important to realize that the Scherrer

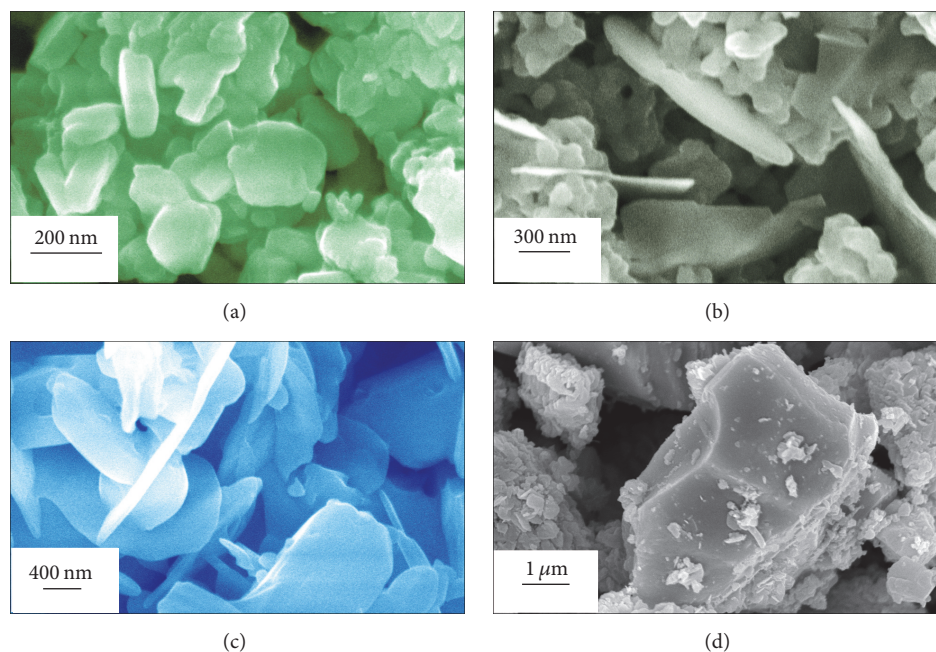


FIGURE 3: SEM micrographs of the precursors after thermal annealing at 200°C (a), 400°C (b), 600°C (c), and 800°C (d). The luminescent materials in (a) is Eu^{3+} doped $\text{Zn}_5\text{Mo}_2\text{O}_{11}\cdot 5\text{H}_2\text{O}$ whilst those in (b–d) are Eu^{3+} doped ZnMoO_4 compounds.

formula provides a lower bound on the particle size. The Scherrer equation is limited to nanoscale particles only; it is not accurately applicable to grains larger than about 200 nm. The reason for this is that a variety of factors can contribute to the width of a diffraction peak besides instrumental effects and crystallite size; the most important of these are usually inhomogeneous strain and crystal lattice imperfections.

The most prominent result in Figures 1 and 2 is that Eu^{3+} doped ZMO can be converted into Eu^{3+} doped ZnMoO_4 at a specific temperature between 200 and 400°C. The ZnMoO_4 belongs to the triclinic crystal system with space group $\text{P}\bar{1}$. One unit cell of triclinic ZnMoO_4 is composed of six molecular weights of ZnMoO_4 [9]. In the ZnMoO_4 structure, the Mo^{6+} ions occupy three nonequivalent positions being surrounded by four oxygen ions with approximately tetrahedral coordination; meanwhile Zn^{2+} ions occupy sites with 5- and 6-fold coordination. As we know, the ionic radius of Eu^{3+} ($r = 94.7$ pm when coordination number (CN) = 6) is close to that of Zn^{2+} ($r = 90$ pm when CN = 6) [5]. Therefore, the four coordinated Mo^{6+} ($r = 41$ pm when CN = 4) sites are too small for Eu^{3+} ($r = 94.7$ pm) to occupy. Thus we believe that Eu^{3+} ions prefer to occupy the Zn^{2+} site. That is the reason why the diffraction patterns of the ZnMoO_4 are not affected too much by Eu^{3+} doping at the concentration of 1 mol%.

3.2. SEM Characterization. Figure 3 shows the SEM micrographs of the as-prepared precursors after thermal annealing at 200°C (a), 400°C (b), 600°C (c), and 800°C (d), respectively. The luminescent materials in (a) are Eu^{3+} doped ZMO whilst those in (b–d) are Eu^{3+} doped ZnMoO_4 compounds. As shown in Figure 3(a), the size of Eu^{3+} doped ZMO

nanoparticles varies from 20 to 200 nm. Figure 3(b) shows that the Eu^{3+} doped ZnMoO_4 nanostructures are a mixture of nanoparticles and nanoplates when the sintering temperature is 400°C. The typical side length of the nanoplates is around 300 nm whilst the thickness of the nanoplates varies from 20 to 50 nm. If the sintering temperature is increased further to 600°C, Eu^{3+} doped ZnMoO_4 nanoplates are formed. As illustrated in Figure 3(c), all nanoparticles are converted into nanoplates whose well-defined crystal facets can be clearly seen. The typical thickness of Eu^{3+} doped ZnMoO_4 nanoplates is around 20–90 nm, and their side length ranges from 300 nm to 1 μm . When the sintering temperature is elevated to 800°C, the Eu^{3+} doped ZnMoO_4 phosphors are developed into micrometer-sized crystals. The largest size of the Eu^{3+} doped ZnMoO_4 microcrystal is around 10 μm . It is worth noting that the melting temperature of ZnMoO_4 is $1003 \pm 5^\circ\text{C}$ and the crystallization temperature of its melt is $975 \pm 5^\circ\text{C}$. So bulk crystal is formed when the sintering temperature is higher than 1000°C , which is not shown here. The data in Figure 3 demonstrate that the morphology of Eu^{3+} doped ZnMoO_4 is highly dependent on the sintering temperature. Particularly, it is found that ZnMoO_4 nanoplates can result when the sintering temperature is in the range of 400 and 600°C, suggesting that there is a preferential direction of crystal growth. Peng et al. proposed a schematic diagram to illustrate the formation of ZnMoO_4 nanoplates [11]. Moreover, as has been observed in Figure 3, the size of Eu^{3+} doped ZnMoO_4 gets larger when the sintering temperature is higher; meanwhile the surface area of Eu^{3+} doped ZnMoO_4 phosphor is significantly reduced. During the sintering process, atomic diffusion drives powder surface

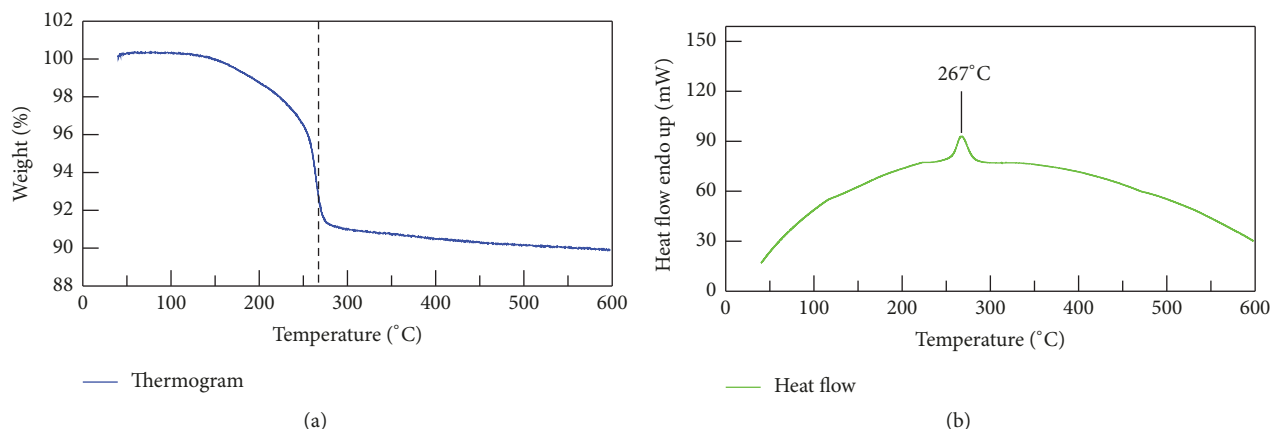


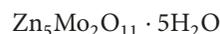
FIGURE 4: TG curve (a) and DSC curve (b) of the Eu^{3+} doped $\text{Zn}_5\text{Mo}_2\text{O}_{11}\cdot 5\text{H}_2\text{O}$.

elimination. The driving force for the densification is the change in free energy from the decrease in surface area and lowering of the surface free energy. As a result of the sintering, new but lower-energy solid-solid interfaces are formed with a total decrease in free energy. This is one of the main reasons why sintering at a higher temperature enlarges the size of Eu^{3+} doped ZnMoO_4 with the result of significantly reduced surface area.

Through the SEM pictures in Figure 3, we calculated the statistics of the particle sizes as a function of temperature. The particle size of ZMO in Figure 3(a) spans from 20 to 200 nm with its most probable size at around 85 nm. After having excluded the large-sized nanoplates from particle size statistics, the particle size of Eu^{3+} doped ZnMoO_4 in Figure 3(b) spans from 20 to 50 nm with its most probable size at around 40 nm. In a similar way, the length of Eu^{3+} doped ZnMoO_4 plates in Figure 3(c) varies from 300 nm to $1\ \mu\text{m}$ with its most probable size at about 420 nm. Finally, the particle sizes of Eu^{3+} doped ZnMoO_4 microcrystals in Figure 3(d) are distributed in the range of 1– $10\ \mu\text{m}$ with their most probable size being about $3\ \mu\text{m}$.

3.3. Thermogravimetric Analysis. TG analysis measures the change in weight of a sample as it is heated. The phase transition from Eu^{3+} doped ZMO to Eu^{3+} doped ZnMoO_4 can be verified by thermogravimetric analysis. Figure 4(a) shows the TG curve of the precursor Eu^{3+} doped ZMO. The samples were heated up to 600°C using a scanning rate of $10^\circ\text{C}/\text{min}$ in the TG and DSC characterizations. From Figure 4(a), one can find that precursor has one distinct weight loss event that occurs at around 250°C during heating from 50 to 600°C . The total weight loss is determined to be 10.45% for Eu^{3+} doped ZMO. The weight loss of the precursor suggests that something happens to the Eu^{3+} doped ZMO. DSC measures the heat difference with the change of temperature, so a direct evidence for the phase transition can be given by the DSC analysis. Figure 4(b) is the DSC curve of the Eu^{3+} doped ZMO. As shown by Figure 4(b), there is a sharp peak at about 267°C when Eu^{3+} doped ZMO is heated from 50 to 600°C , indicating that the phase transition takes

place at around 267°C . Based on the TG and DSC results along with the XRD data in Figures 1 and 2, the formation processes of Eu^{3+} doped ZMO could be summarized by the following reaction scheme:



Equation (1) describes the hydrolysis of the molybdenum salt in the basic solution whilst (2) illustrates the formation of ZMO. Upon heating, ZMO undergoes a reaction where hydrate is released from the material when sintering at a temperature higher than 267°C . Our recorded weight loss (10.45%) is extremely comparable with the theoretical value of water in ZMO (11.5%). Therefore, the weight loss of the precipitate in Figure 4 can be attributed to the decomposition of Eu^{3+} doped ZMO at 267°C . Besides the characterizations in nitrogen, we performed the TG and DSC characterizations for the sample under air purge gas at the heating rate of $10^\circ\text{C}/\text{min}$. No obvious differences were recorded in the TG/DSC curves when measured in air and in nitrogen. The reason for the no differences rests on the fact that our sample is inert to both oxygen and nitrogen.

3.4. PL Spectral Analysis. Figure 5 displays the PL spectra of Eu^{3+} doped ZMO after thermal annealing at 200, 400, 600, and 800°C for 2 h. The luminescent materials in (a) are the Eu^{3+} doped ZMO whilst those in (b–d) are Eu^{3+} doped ZnMoO_4 compounds. Each PL spectrum consists of broadband emissions centered at around 550 nm and a series of sharp emissions peaking at 592, 612, and 650 nm. After the Eu^{3+} doped ZMO has been annealed at 200°C for 2 h, the sharp emissions in Figure 5(a) peak at 592, 612, and 650 nm, corresponding to the electronic transitions $^5\text{D}_0 \rightarrow ^7\text{F}_1$, $^5\text{D}_0 \rightarrow ^7\text{F}_2$, and $^5\text{D}_0 \rightarrow ^7\text{F}_3$ of Eu^{3+} ions in the host ZMO [4–6]. Figure 5(b) shows that quite similar PL spectrum has

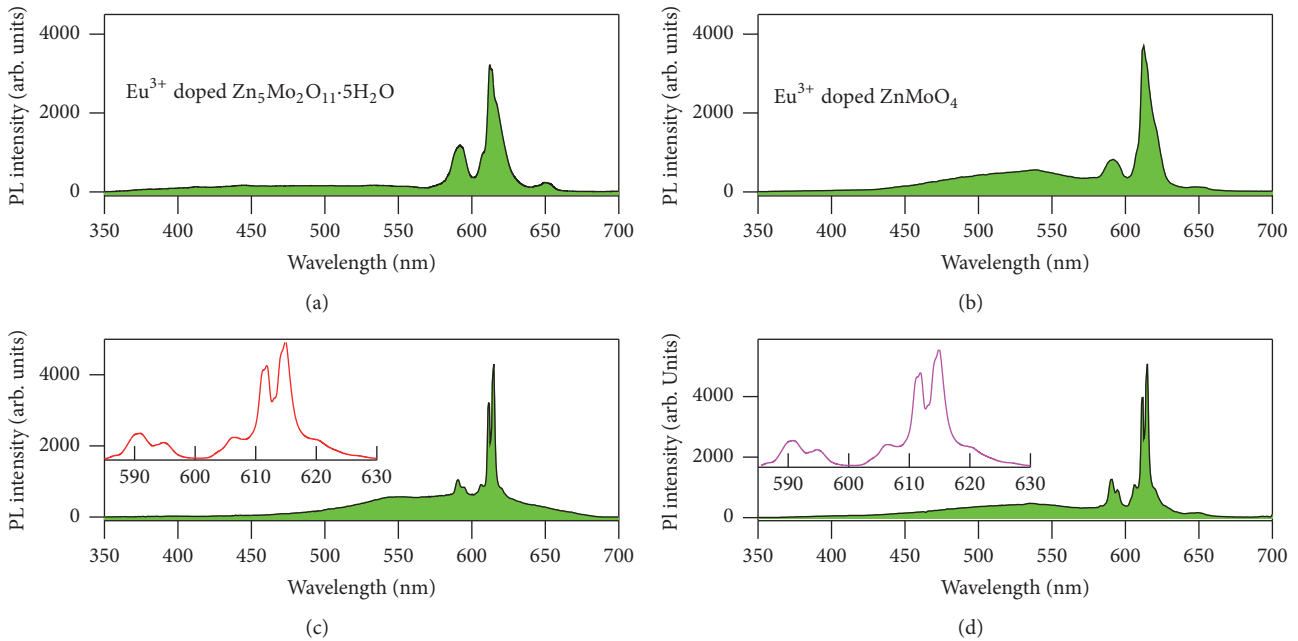


FIGURE 5: PL spectra of the precursors after thermal annealing at 200°C (a), 400°C (b), 600°C (c), and 800°C (d). The luminescent materials in (a) are the Eu^{3+} doped $\text{Zn}_5\text{Mo}_2\text{O}_{11}\cdot 5\text{H}_2\text{O}$ whilst those in (b–d) are Eu^{3+} doped ZnMoO_4 compounds. Inset: a zoom in the region 585–630 nm to show the split emissions of transitions ${}^5\text{D}_0 \rightarrow {}^7\text{F}_1$ and ${}^5\text{D}_0 \rightarrow {}^7\text{F}_2$.

been recorded for Eu^{3+} doped ZnMoO_4 . The most important feature in Figures 5(a) and 5(b) is that the transition ${}^5\text{D}_0 \rightarrow {}^7\text{F}_2$ (at 612 nm) is strong whilst the other two transitions ${}^5\text{D}_0 \rightarrow {}^7\text{F}_1$ (at 592 nm) and ${}^5\text{D}_0 \rightarrow {}^7\text{F}_3$ (at 650 nm) are relatively weak. As is well known, the ${}^5\text{D}_0 \rightarrow {}^7\text{F}_1$ line originates from magnetic dipole transition whilst the ${}^5\text{D}_0 \rightarrow {}^7\text{F}_2$ line results from the electric dipole transition. In terms of the Judd–Ofelt theory, the magnetic dipole transition is permitted, but the electric dipole transition is allowed only on condition that the Eu ion occupies a site without an inversion center. Subsequently, the ${}^5\text{D}_0 \rightarrow {}^7\text{F}_1$ transitions should be relatively strong if Eu^{3+} ions occupy inversion center sites. Otherwise, the ${}^5\text{D}_0 \rightarrow {}^7\text{F}_2$ transitions should be strong when Eu^{3+} occupies a center of asymmetry in the host lattice. The results in Figures 5(a) and 5(b) indicate that most of Eu^{3+} ions do not occupy inversion center sites either in ZMO or in ZnMoO_4 . The lack of inversion symmetry and the break of parity selection rules in ZMO and ZnMoO_4 make the ${}^5\text{D}_0 \rightarrow {}^7\text{F}_2$ electric dipole transition strongest among all these transitions.

The second most important feature shared by Figures 5(a) and 5(b) is that the transitions ${}^5\text{D}_0 \rightarrow {}^7\text{F}_1$ and ${}^5\text{D}_0 \rightarrow {}^7\text{F}_2$ of Eu^{3+} in Figures 5(a) and 5(b) are structureless. After substituting the Zn^{2+} sites in ZnMoO_4 , Eu^{3+} ions in the ZnMoO_4 crystal lattice experience different crystal field strength due to the different chemical environments around the substitution sites. There are, in fact, multiple emission lines that can be expected in each PL spectrum due to the crystal field splitting of the ground state of the Eu^{3+} ions. A literature survey reveals that the splitting of the characteristic emissions of Eu^{3+} ions is not well considered for rare-earth doped ZnMoO_4 [4–8],

but line splitting has been reported in Eu^{3+} doped tellurite glasses [12], double borate $\text{Ca}_3\text{Gd}_2(\text{BO}_3)_4$ [13], NaYP_2O_7 [14], and $\text{Y}_2\text{Sn}_2\text{O}_7$ [15]. Although the splitting of the characteristic emissions of Eu^{3+} are not observed in Figure 4(b) for Eu^{3+} ZnMoO_4 , suggesting that the local crystal fields around the Eu^{3+} sites are not distinctly differentiated. Fortunately, the splitting of the characteristic emission of Eu^{3+} can be observed when the sintering temperature is 600°C or higher. As depicted in Figures 5(c) and 5(d), the characteristic emission of Eu^{3+} at 612 nm is split into four fine lines peaking at 606, 611, 615, and 620 nm; meanwhile the emission at 592 nm is split into two fine lines peaking at 590 and 595 nm. Zooms in the region 585–630 nm are shown as insets in Figures 5(c) and 5(d) to show the emission splitting of the transitions ${}^5\text{D}_0 \rightarrow {}^7\text{F}_1$ and ${}^5\text{D}_0 \rightarrow {}^7\text{F}_2$. The energy difference between the two split lines of the transitions ${}^5\text{D}_0 \rightarrow {}^7\text{F}_1$ is 142 cm^{-1} whereas those of the split lines of the transitions ${}^5\text{D}_0 \rightarrow {}^7\text{F}_2$ are 135, 106, and 131 cm^{-1} , respectively. The splitting of the Eu^{3+} emissions can be thought of as a consequence of the change in the local environment; thus the splitting of Eu^{3+} emissions in ZnMoO_4 suggests a sufficient variation in the local crystal field around Eu^{3+} ions in ZnMoO_4 . We can see that sintering is effective in changing the local crystal field around the rare-earth ions [16].

The third most important feature in Figure 5 rests on the fact that a broadband emission appears in each PL spectrum with its center at around 550 nm. We can attribute it to the intrinsic defects in Eu^{3+} doped hosts. Generally speaking, photoexcitation creates electrons in the conduction band and holes in the valence band of Eu^{3+} doped ZMO and

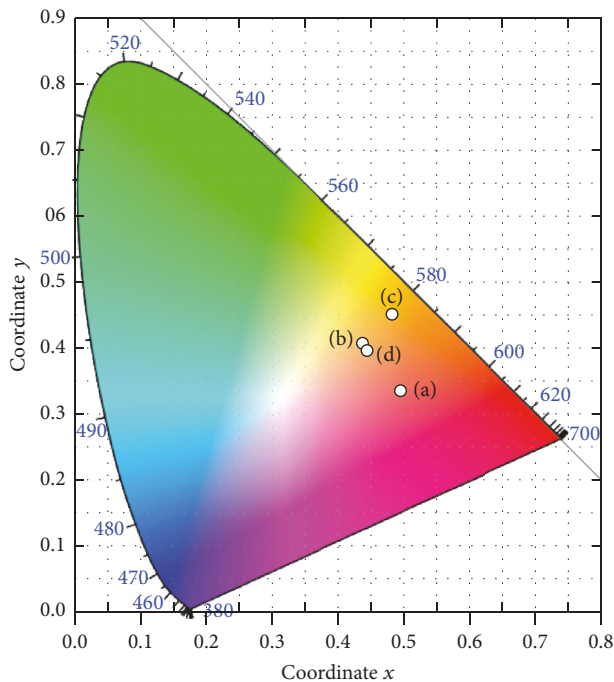


FIGURE 6: CIE chromaticity diagram of the colored PL from the precursors after thermal annealing at 200°C (a), 400°C (b), 600°C (c), and 800°C (d). The luminescent materials in (a) are Eu^{3+} doped $\text{Zn}_5\text{Mo}_2\text{O}_{11}\cdot 5\text{H}_2\text{O}$ whilst those in (b–d) are Eu^{3+} doped ZnMoO_4 compounds.

Eu^{3+} doped ZnMoO_4 ; then the photoexcited carriers are relaxed through the band-edge free excitonic recombination or through the intrinsic defects in the hosts. In the case of ZnMoO_4 , the band-edge excitonic recombination can be excluded since the bandgap of ZnMoO_4 is about 4 eV [9, 10]. Consequently, the defects in ZnMoO_4 should be the candidate of the broadband PL centered at about 550 nm. As we know, Zn, O, and Mo vacancies are the most common intrinsic defects in ZnMoO_4 . At the current stage, we may tentatively assign the broadband PL centered at about 550 nm to these intrinsic vacancies in ZnMoO_4 .

Color coordinates are important parameters to quantitatively describe the emission color for luminescent materials, and the CIE chromaticity coordinates can be calculated from the PL spectral data of luminescent materials [17–20]. Figure 6 represents the CIE chromaticity diagram of the PL color of thermally annealed ZMO at 200°C (a), 400°C (b), 600°C (c), and 800°C (d). The luminescent materials in (a) are Eu^{3+} doped ZMO whilst those in (b–d) are Eu^{3+} doped ZnMoO_4 compounds. As shown in Figure 6, the color coordinates are (0.495, 0.335), (0.437, 0.407), (0.482, 0.451), and (0.444, 0.396) when the Eu^{3+} doped ZMO is thermally annealed at 200, 400, 600, and 800°C, respectively. Accordingly, the luminescent color is pink for the Eu^{3+} doped ZMO after annealing at 200°C for 2 h; meanwhile the luminescent color is yellowish orange when the Eu^{3+} doped ZMO is annealed at 400, 600, and 800°C for 2 h. Although the luminescent color of Eu^{3+} doped ZMO is different from

that of Eu^{3+} doped ZnMoO_4 , it is clear that the PL color of Eu^{3+} doped ZnMoO_4 varies not too much with the annealing temperature.

3.5. EDX and PL Excitation Spectra of $\text{ZnMoO}_4:\text{Eu}^{3+}$. It is important to demonstrate the presence of Eu^{3+} ions in Eu^{3+} doped ZnMoO_4 . EDX is an analytical technique used for the elemental analysis of a specimen. Figure 7(a) depicts the EDX spectrum of Eu^{3+} doped ZnMoO_4 nanoplates. The Eu^{3+} doped ZnMoO_4 nanoplates are derived by sintering the Eu^{3+} doped ZMO at 600°C for 2 h. As can be seen in Figure 7, the X-ray emission peaks are located at 0.53, 1.02, 2.30, 8.61, and 9.57 keV, corresponding to the characteristic X-ray emissions of O($\text{K}\alpha_{1,2}$), Zn($\text{L}\alpha_{1,2}$), Mo($\text{L}\alpha_1$), Zn($\text{K}\alpha_1$), and Zn($\text{K}\beta_{1,3}$), respectively. These data indicate the presence of Zn, O, and Mo in the phosphor, which is consistent with the XRD analysis. In particular, we also recorded the X-ray emission peaks of element Eu in the sample. As marked by the vertical arrows in Figure 7(a), the X-ray emission peaks at 5.85 and 6.46 keV can be assigned to $\text{Eu}(\text{L}\alpha_1)$ and $\text{Eu}(\text{L}\beta_1)$, respectively.

Due to its superior signal-to-noise ratio, PL excitation spectroscopy is one useful method to investigate the electronic levels of materials with low absorption. Figure 7(b) depicts the PL excitation spectrum of Eu^{3+} doped ZnMoO_4 nanoplates that are derived by sintering the precursor at 600°C for 2 h. The monitoring wavelength was fixed at 615 nm. It can be seen in Figure 7(b) that the PL excitation spectrum consists a broadband centered at about 300 nm and some sharp absorption peaks. The broad excitation band from 220 to 350 nm is ascribed to the O-Mo charge transfer transition whereas the sharp lines in the 360–500 nm range are intraconfigurational $4f-4f$ transitions of Eu^{3+} ions in the host lattice. Additionally, the broad excitation band from 220 to 350 nm could partly be attributed to the O-Eu charge transfer transition. On one hand, the strong excitation peaks at 393 and 464 nm can be attributed to the ${}^7\text{F}_0 \rightarrow {}^5\text{L}_6$ and ${}^7\text{F}_0 \rightarrow {}^5\text{D}_2$ transitions of Eu^{3+} , respectively. On the other hand, the three weak peaks at 361, 381, and 413 nm can be attributed to the transitions from ${}^7\text{F}_0$ to ${}^5\text{D}_4$, ${}^5\text{L}_7$, and ${}^5\text{D}_3$, respectively [4–6]. These characteristic transitions indicate that the Eu^{3+} ions are incorporated into ZnMoO_4 .

3.6. Absorption Spectra of $\text{ZnMoO}_4:\text{Eu}^{3+}$. Doping ZnMoO_4 with Eu^{3+} ions introduces extra defects in the host material. Figure 8 shows the absorption spectra of the undoped ZnMoO_4 and Eu^{3+} doped ZnMoO_4 nanoplates. The undoped ZnMoO_4 was utilized as a control sample. Both the undoped ZnMoO_4 and Eu^{3+} doped ZnMoO_4 nanoplates were derived by sintering their precursors at 600°C for 2 h. It can be seen in Figure 8 that two absorption bands are present in each curve, among which one starts its absorption in the range 310–390 nm whilst the other starts its absorption in the range 250–310 nm. When compared to the transmission spectrum of ZnMoO_4 single crystals [1], we can assign the strong absorption band in the range of 310–390 nm to defects in ZnMoO_4 ; meanwhile we can assign the intense absorption in the range of 250–310 nm to the electron transition from

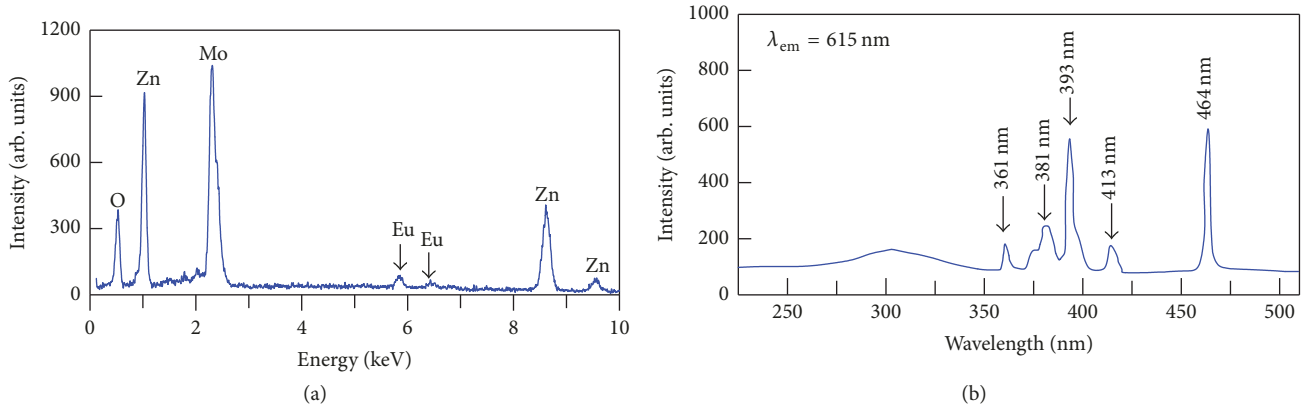


FIGURE 7: EDX spectrum (a) and PL excitation spectrum (b) of the precursor after thermal annealing at 600°C for 2 h. The luminescent materials in (a) and (b) are Eu^{3+} doped ZnMoO_4 nanoplates.

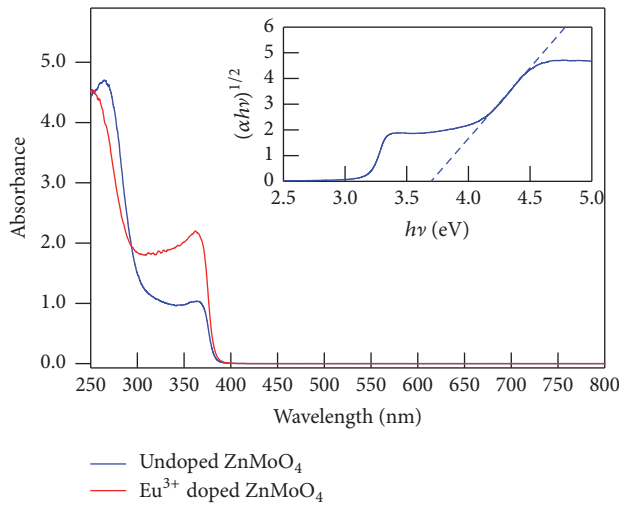
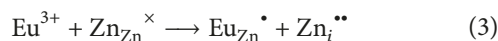


FIGURE 8: Absorption spectra of undoped ZnMoO_4 (blue curves) and Eu^{3+} doped ZnMoO_4 (red curves). The undoped ZnMoO_4 and Eu^{3+} doped ZnMoO_4 nanoplates were derived by sintering their precursors at 600°C for 2 h, respectively. Inset: Tauc plot of the undoped ZnMoO_4 obtained by sintering its precursor at 600°C for 2 h.

the valence band to the conduction of the ZnMoO_4 . Thus, Figure 8 shows clearly that doping ZnMoO_4 with Eu^{3+} ions can significantly increase the population density of the defects in the host. Assuming that the cation Eu has +3 charge, the Kröger-Vink notation for the defect reactions of Eu^{3+} in ZnMoO_4 can be described by the following equation:



In (3), the masses, sites, and charges are balanced for both intrinsic and extrinsic defects. Equation (3) indicates that an Eu^{3+} ion substitutes one Zn site in ZnMoO_4 , yielding one positively charged defect $\text{Eu}_{\text{Zn}}^{\bullet}$ and another positively charged interstitial defect $\text{Zn}_i^{\bullet\bullet}$. Thus doping ZnMoO_4 with Eu^{3+} ions can significantly increase the population density of the defects in the host. On the other hand, triclinic ZnMoO_4

is an indirect semiconductor [9]. In a parabolic band structure, the optical bandgap and absorption coefficient of an indirect semiconductor can be calculated by

$$\alpha h\nu = C_1 (h\nu - E_g)^2, \quad (4)$$

where α is the linear absorption coefficient of the material, $h\nu$ is the photon energy, C_1 is a proportionality constant, and E_g is the optical bandgap. The inset of Figure 8 shows the plot of $(\alpha h\nu)^{1/2}$ against $h\nu$ for the undoped ZnMoO_4 . The optical bandgap value of the undoped ZnMoO_4 nanoplates can be calculated to be 3.70 eV. This optically derived bandgap value agrees roughly with the theoretically calculated bandgap value of 3.79 eV [9]. A quite similar bandgap value (3.72 eV) is derived for Eu^{3+} doped ZnMoO_4 nanoplates. Moreover, we note that the absorption in the inset starts at about 3.1 eV. As documented in the literature, the bandgap value of ZnMoO_4 was estimated in the range of 4.17–5.35 eV on the basis of the luminescence excitation and reflectivity spectra [9]. In our case, the intensity of the absorption band in the range of 310–390 nm can be effectively modified by Eu^{3+} doping, as shown in Figure 8. Consequently, we tentatively assign this absorption band to defects in ZnMoO_4 .

3.7. Time-Resolved PL of $\text{ZnMoO}_4:\text{Eu}^{3+}$ Nanocrystals. As discussed above, the broad PL band centered at about 550 nm belongs to the intrinsic defect emission whereas the characteristic emission of Eu^{3+} at 615 nm can be classified as the extrinsic defect emission. Quantitatively speaking, the two kinds of emissions should have different decay behaviors. Figure 9 depicts the semilogarithmic plots of the room temperature PL decay curve of Eu^{3+} doped ZnMoO_4 nanoplates under the excitation of 375 nm. The Eu^{3+} doped ZnMoO_4 nanoplates were derived by sintering the precipitate at 600°C for 2 h. The emission wavelength for the PL decay in Figure 9(a) was monitored at 550 nm, while the emission wavelength for the PL decay in Figure 9(b) was fixed at 615 nm. It can be seen in Figure 9(a) that the PL decay profile exhibits double exponential nature. The best fit to the experimental data in Figure 9(a) can be obtained using two

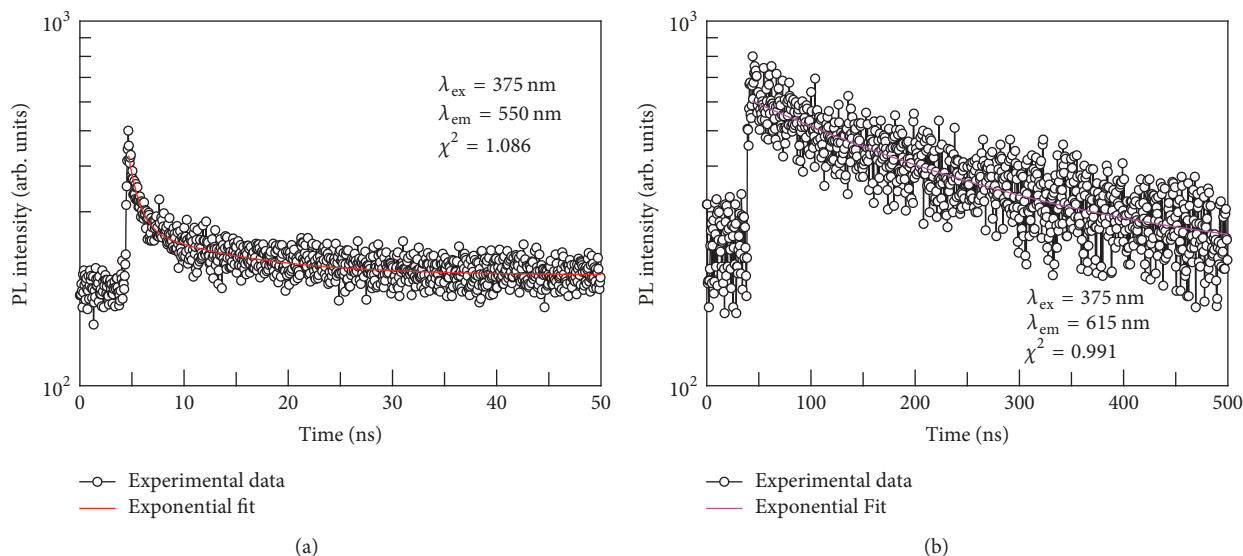


FIGURE 9: Time-resolved PL spectra of ZnMoO₄:Eu³⁺ derived by sintering the precursor at 600°C for 2 h. The emission wavelength was fixed at 550 nm (a) and 615 nm (b), respectively.

exponentials with the decay time constants $\tau_1 = 0.96 \pm 0.11$ ns and $\tau_2 = 10.23 \pm 1.09$ ns. It is noted that τ_1 is at the limit of the measurement capabilities of the instrument and therefore it merely represents the order of the short decay time constant. When compared to the long PL lifetime (3.9 μ s) of the ZnMoO₄ single crystals grown by the Czochralski method [2], the observation of the quite short PL decay time for our Eu³⁺ doped ZnMoO₄ nanoplates gives further evidence on the defect emission at 550 nm for the Eu³⁺ doped ZnMoO₄ nanoplates. As shown in Figure 9(b), the PL decay profile of Eu³⁺ doped ZnMoO₄ nanoplates exhibits single exponential nature. The best fit to the experimental data in Figure 9(b) can be obtained using one exponential with the decay time constants $\tau_1 = 218.29 \pm 17.57$ ns for the PL emission at 615 nm. A comparison of the two decay curves in Figure 9 demonstrates that the PL decay behavior of the broad PL band centered at about 550 nm is dramatically different from that of the characteristic emission of Eu³⁺ at 615 nm.

4. Conclusions

The effects of sintering temperature on the crystal structure, morphology, and PL properties of the precursor are investigated; both the morphology and the PL spectrum of Eu³⁺ doped ZnMoO₄ nanocrystals are found to be highly dependent on the sintering temperature of the precursor. XRD, SEM, and thermogravimetric analyses have shown that Eu³⁺ doped ZnMoO₄ nanostructures can be derived by controlling the annealing temperature in the range of 267–800°C. As the sintering temperature increases from 267 to 800°C, the morphology of Eu³⁺ doped ZnMoO₄ evolves from nanoparticles at 400°C to nanoplates at 600°C and eventually to microcrystals at 800°C. Moreover, a broad PL band with its center at around 560 nm is recorded for Eu³⁺ doped ZnMoO₄; the characteristic emissions of Eu³⁺ at 592

and 612 nm are split into several fine lines when the sintering temperature is beyond 600°C. Our results have demonstrated that Eu³⁺ doped ZnMoO₄ can be derived cost-effectively by sintering the precursor of Eu³⁺ doped ZMO at a relatively low temperature of about 400°C.

Conflicts of Interest

The authors declare that they have no conflicts of interest.

Acknowledgments

The authors would like to acknowledge the financial support from National Natural Science Foundation of China (nos. 11574036, 11304025, and 11604028).

References

- [1] D. Spassky, A. Vasil'Ev, I. Kamenskikh et al., "Luminescence investigation of zinc molybdate single crystals," *Physica Status Solidi (a)—Applications and Materials Science*, vol. 206, no. 7, pp. 1579–1583, 2009.
- [2] V. B. Mikhailik, H. Kraus, D. Wahl, H. Ehrenberg, and M. S. Mykhaylyk, "Optical and luminescence studies of ZnMoO₄ using vacuum ultraviolet synchrotron radiation," *Nuclear Instruments and Methods in Physics Research Section A: Accelerators, Spectrometers, Detectors and Associated Equipment*, vol. 562, no. 1, pp. 513–516, 2006.
- [3] D. A. Spassky, V. V. Mikhailin, A. E. Savon, E. N. Galashov, V. N. Shlegel, and Y. V. Vasiliev, "Low temperature luminescence of ZnMoO₄ single crystals grown by low temperature gradient Czochralski technique," *Optical Materials*, vol. 34, no. 11, pp. 1804–1810, 2012.
- [4] L.-Y. Zhou, J.-S. Wei, F.-Z. Gong, J.-L. Huang, and L.-H. Yi, "A potential red phosphor ZnMoO₄:Eu³⁺ for light-emitting diode

- application,” *Journal of Solid State Chemistry*, vol. 181, no. 6, pp. 1337–1341, 2008.
- [5] A. Xie, X. Yuan, F. Wang, Y. Shi, and Z. Mu, “Enhanced red emission in $\text{ZnMoO}_4:\text{Eu}^{3+}$ by charge compensation,” *Journal of Physics D: Applied Physics*, vol. 43, no. 5, Article ID 055101, 2010.
- [6] L. Yu and M. Nogami, “The synthesis and photoluminescent properties of one-dimensional $\text{ZnMoO}_4:\text{Eu}^{3+}$ nanocrystals,” *Materials Letters*, vol. 64, no. 14, pp. 1644–1646, 2010.
- [7] T. Chengaiah, C. K. Jayasankar, K. Pavani, T. Sasikala, and L. R. Moorthy, “Preparation and luminescence characterization of $\text{Zn}_{(1-x)}\text{MoO}_4:\text{XDy}^{3+}$ phosphor for white light-emitting diodes,” *Optics Communications*, vol. 312, pp. 233–237, 2014.
- [8] X. Ju, X. Li, W. Li, W. Yang, and C. Tao, “Luminescence properties of $\text{ZnMoO}_4:\text{Tb}^{3+}$ green phosphor prepared via coprecipitation,” *Materials Letters*, vol. 65, no. 17–18, pp. 2642–2644, 2011.
- [9] D. A. Spassky, A. N. Vasil’Ev, I. A. Kamenskikh et al., “Electronic structure and luminescence mechanisms in ZnMoO_4 crystals,” *Journal of Physics: Condensed Matter*, vol. 23, no. 36, Article ID 365501, 2011.
- [10] B.-G. Zhai, Q.-L. Ma, L. Yang, and Y. M. Huang, “Growth of ZnMoO_4 nanowires via vapor deposition in air,” *Materials Letters*, vol. 188, pp. 119–122, 2017.
- [11] C. Peng, L. Gao, S. Yang, and J. Sun, “A general precipitation strategy for large-scale synthesis of molybdate nanostructures,” *Chemical Communications*, no. 43, pp. 5601–5603, 2008.
- [12] C. Cascales, R. Balda, J. Fernández, M. A. Arriandiaga, and J. M. Fdez-Navarro, “Fluorescence line narrowing spectroscopy of Eu^{3+} in $\text{TeO}_2\text{-TiO}_2\text{-Nb}_2\text{O}_5$ glass,” *Optical Materials*, vol. 31, no. 7, pp. 1092–1095, 2009.
- [13] H. J. Seo, “Line broadening and crystallographic sites for Eu^{3+} in disordered double borate $\text{Ca}_3\text{Gd}_2(\text{BO}_3)_4$,” *Journal of Alloys and Compounds*, vol. 604, pp. 100–105, 2014.
- [14] S. M. V. Novais and Z. S. Macedo, “Local atomic arrangement and scintillation properties of Eu- and Ce-doped NaY_2O_7 ,” *Journal of Solid State Chemistry*, vol. 233, pp. 103–107, 2016.
- [15] A. Ege, M. Ayvacikli, O. Dinçer, and S. U. Satılmış, “Spectral emission of rare earth (Tb, Eu, Dy) doped $\text{Y}_2\text{Sn}_2\text{O}_7$,” *Journal of Luminescence*, vol. 143, pp. 653–656, 2013.
- [16] G. Torsello, M. Lomascolo, A. Licciulu, D. Diso, S. Tundo, and M. Mazzer, “The origin of highly efficient selective emission in rare-earth oxides for thermophotovoltaic applications,” *Nature Materials*, vol. 3, no. 9, pp. 632–637, 2004.
- [17] Q.-L. Ma, R. Xiong, and Y. M. Huang, “Tunable photoluminescence of porous silicon by liquid crystal infiltration,” *Journal of Luminescence*, vol. 131, no. 10, pp. 2053–2057, 2011.
- [18] Q.-L. Ma, B.-G. Zhai, and Y. M. Huang, “Sol-gel derived ZnO /porous silicon composites for tunable photoluminescence,” *Journal of Sol-Gel Science and Technology*, vol. 64, no. 1, pp. 110–116, 2012.
- [19] Q.-L. Ma, B.-G. Zhai, and Y. M. Huang, “Dopant concentration dependent photoluminescence and afterglow of $\text{SrAl}_2\text{O}_4:\text{Dy}^{3+}$ phosphors,” *Materials Research Innovations*, vol. 19, pp. s40–s44, 2015.
- [20] B.-G. Zhai, L. Yang, Q.-L. Ma, X. Liu, and Y. M. Huang, “Mechanism of the prolongation of the green afterglow of $\text{SrAl}_2\text{O}_4:\text{Dy}^{3+}$ caused by the use of H_3BO_3 flux,” *Journal of Luminescence*, vol. 181, pp. 78–87, 2017.



Hindawi
Submit your manuscripts at
www.hindawi.com

